The Visible Nulling Coronagraph-- Architecture Definition and Technology Development Status

B. Martin Levine[1], Francisco Aguayo[1], Thomas Bifano[2,3], S. Felipe Fregoso[1], Joseph J. Green[1], Benjamin F. Lane[4], Duncan T. Liu[1], Bertrand Mennesson[1], Shanti Rao[1], Rocco Samuele[5], Michael Shao[1], Edouard Schmidtlin[1], Eugene Serabyn[1], Jason Stewart[6], and J. Kent Wallace[1]

Abstract

We describe the advantages of a nulling coronagraph instrument behind a single aperture space telescope for detection and spectroscopy of Earth-like extrasolar planets in visible light. Our concept synthesizes a nulling interferometer by shearing the telescope pupil into multiple beams. They are recombined with a pseudo-achromatic pi-phase shift in one arm to produce a deep null on-axis, attenuating the starlight, while simultaneously transmitting the off-axis planet light. Our nulling configuration includes methods to mitigate stellar leakage, such as spatial filtering by a coherent array of single mode fibers, balancing amplitude and phase with a segmented deformable mirror, and post-starlight suppression wavefront sensing and control. With diffraction limited telescope optics and similar quality components in the optical train (λ/20), suppression of the starlight to 10^{-10} is readily achievable. We describe key features of the architecture and analysis, present the status of key experiments to demonstrate wide bandwidth null depth, and present the status of component technology development.

Keywords: Extra-solar Planet Detection, High Contrast Imaging, Nulling Interferometer, Coronagraph, Post-suppression Wavefront Sensing, Space Instrumentation

1. Introduction

The objectives are to develop a nulling coronagraph based imager and spectrometer concept that will increase the number of planets the Terrestrial Planet Finder-Coronagraph (TPF-C) detects (Coulter, 2004), and to expand the wavelength range of the spectrometer into the near-IR to enable detection of additional unique visible biomarkers. This instrument utilizes an alternative starlight suppression system (SSS) based on the principles of nulling interferometry, which allows inner working angles (IWA) within 2-3 λ/D to be obtained, and also to measure low resolution (R=80) spectra. Equally important, this concept contains a post starlight suppression wavefront sensor (or calibration wavefront sensor) to increase the achievable contrast level, and to substantially decrease stability requirements during integration (Shao, 2006).

The nulling coronagraph can, in theory, achieve the required $1x10^{-10}$ suppression of starlight within an IWD of 2 λ/D. Coverage of the 0.5 ~1.7 μm wavelength range is done in intervals of 25% bandwidth. The search for planets will be conducted at short wavelengths, where the IWA is smaller. Extending spectroscopy to 1.7μm, the visible and near infra-red signatures of likely atmospheric constituents include oxygen, ozone, water, methane, and carbon dioxide, some combinations of which are considered to be biosignatures.

This paper is divided into sections on Concept Description, Concept Analysis, and Technology Overview. The Concept Definition Section briefly describes the basic principles of the nulling coronagraph instrument and why it is capable of making detections at smaller IWA's. It contains a description of the Calibration wavefront sensor, or the estimation of post-SSS wavefront errors by amplitude and phase measurement of the stellar leakage. The next section contains a description of the instrument concepts which includes computation of the expected Signal to Noise ratios for various detection targets. The last section is a broad survey of the state of technology needed to build the nulling coronagraph. Progress toward achieving deep achromatic nulls is shown as well as progress updates on efforts to fabricate coherent fiber optic array assemblies, segmented deformable mirrors, and its associated electronics.

[1] NASA/Jet Propulsion Laboratory, Pasadena CA, [2] Manufacturing Engineering Department, Boston University, Boston, MA, [3.] Boston Micromachines Corporation, Watertown, MA, [4.] MIT Center for Space Research, Cambridge, MA, [5.], Northop-Grumman Space Technology Corporation, Redondo Beach, CA, [6.] Electrical and Computer Engineering Department, Boston University, Boston, MA.

Space Telescopes and Instrumentation I: Optical, Infrared, and Millimeter,
edited by John C. Mather, Howard A. MacEwen, Mattheus W.M. de Graauw,
Proc. of SPIE Vol. 6265, 62651A, (2006) · 0277-786X/06/$15 · doi: 10.1117/12.672736

2. Nulling Concept and Architecture

2.1. Using a nulling interferometer instrument with a single aperture telescope

In the infrared domain, the nulling interferometer approach is more conventional, however, we apply the principles of nulling interferometry to the visible light domain with a conventional single aperture telescope as an alternate starlight suppression method. A nulling interferometer based instrument is used as a high-contrast imaging system to suppress both diffraction and scattering. (Shao, 1991). In principle, a nulling interferometer effectively projects an interference pattern on the sky over the star-planet system to be imaged (Figure 1). The baseline, s, sets the fringe spacing. They attenuate the starlight and have 100% transmission for planet light when the optical path from the planet is $\lambda/2$ different from the star. For a modest sized aperture, about D=1m, a Jupiter-like planet can be resolved by synthesizing an interferometer with a 30-cm baseline, and at D=8m, an Earth-like planet can be resolved with a 50 cm baseline at λ=500μm wavelength.

The implementation for TPF-C calls for synthesizing two nulling interferometers in series. This arrangement is equivalent to a four element nulling interferometer (the first nulling interferometer produces a deep null fringe pattern, and by directing its output into a second nulling interferometer, the null fringe becomes wider, and minimizes light leakage from the finite diameter of the star, and also from pointing errors.). After nulling, an array of coherent single-mode optical fibers, coupled on both sides with (commercially available) lens arrays is used to filter the effects of any residual stellar leakage (scattering) due to imperfections in the telescope optics and optical train. A simple imaging system after this array forms the final extra-solar planet image.

To introduce an achromatic π-radian phase shift in a different fashion, we use pairs of dielectric plates of differing thicknesses. Solutions for achromatic π-radian phase shifts (to the needed accuracy) exist with two glasses (Figure 2 lower right). Thus, for this experiment, the final layout for the beam combiner consists of identical two-glass pairs of (rotatable) dielectric phase retarders (Morgan et. al., 2000), in each leg of the interferometer. Note that with the combination of common BK7 and Fused Silica optical glasses the theoretical minimum

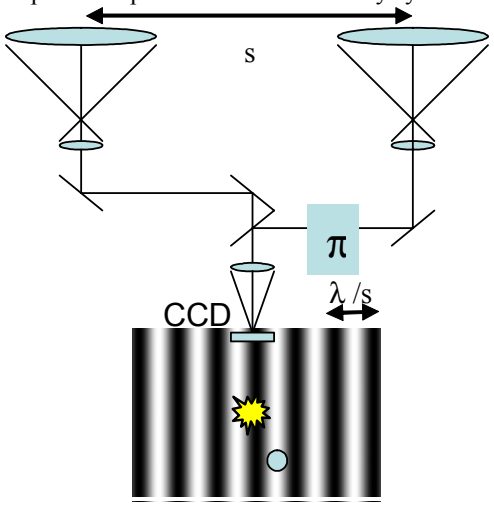

Figure 1. Imaging with nulling interferometry. A fringe pattern is superimposed over the star and planet to be imaged, the star is placed at the bottom of a deep, achromatic destructive (null) fringe, while planet on the constructive fringe is transmitted.

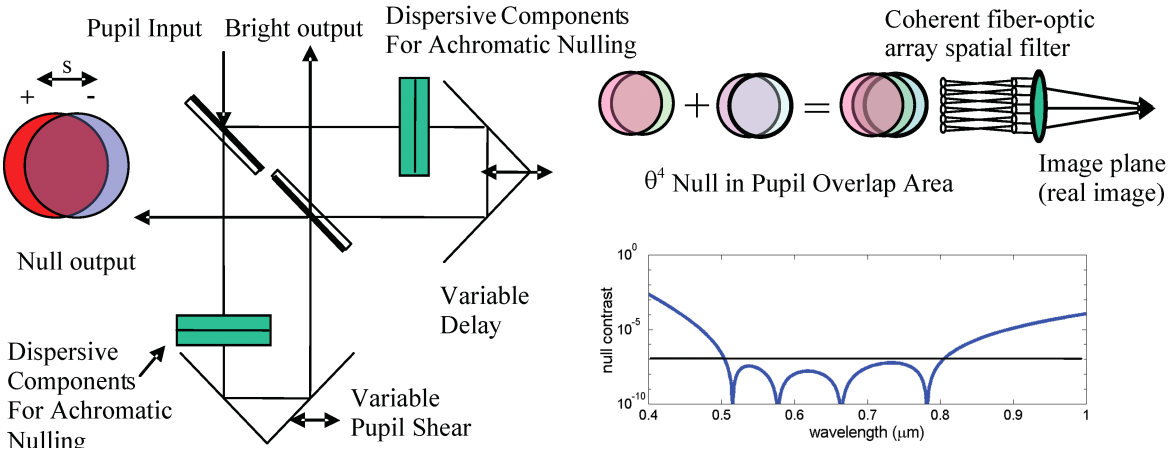

Figure 2. Visible nulling coronagraph instrument concept. Left, a concept for single-input symmetric nulling interferometer. Note that the two pupils emerge from the null output displaced (or sheared) by a distance, s, proportional to the baseline of the instrument. Lower right, Calculation of 'pseudo-achromatic' null using two dielectric plates. Upper right, the major components of nulling coronagraph. By coupling two nulling interferometers, a 4 pupil overlap results in an interference fringe pattern proportional to θ^4. The fiber-optic array is a coherent spatial filter to reject residual scattered light. An imaging system then projects the pupil into the far-field to form an image.

of 10^{-7} can be realized over a 25% bandwidth. In theory, the nulling coronagraph suppresses starlight to 10^{-10} within 1.5~2 λ/D while a more traditional Lyot coronagraph or apodized aperture telescope which has an inner working distance of 3~4 λ/D (Levine et. al., 2003; Wallace, Shao, Levine and Lane, 2003).

2.2. *Spatial Filter Arrays (Figure 3)*

Another advantage of the nulling coronagraph architecture is the single mode fiber array component to provide the deep null required, and also to relax the optical figure quality requirements of the primary telescope optics. With this array of fibers, wavefront errors at high spatial frequency, on a spatial scale smaller than any deformable mirror (DM) actuator, will be filtered by the single-mode fibers instead of propagating to the science focal plane. If the optical fibers all have the same length (to λ/20) the planet light from each fiber combines to form a coherent off-axis image. The phase of the residual star light exiting the fiber array is random, hence it is scattered evenly across the whole field of view. In summary, wavefront errors on a spatial scale larger than the DM actuator spacing are corrected by active control of the DM and wavefront errors smaller than the actuator spacing are filtered by the fiber array.

With an 8-m telescope like for TPF-C, the airy pattern of the telescope has dropped ~10^{-4} by the 5th airy ring, where we expect to find an earth at 10 pc. We need to suppress this by an additional factor of one million to achieve imaging. To keep scattered light below this 10^{-6} level, the optical system would need to be near-perfect (or have a Strehl ratio of 99.9999%), or the scattered light due to any minute optical figure imperfections results in a residual diffraction pattern from a conventional Lyot coronagraph. A Strehl of 10^{-6}, in turn implies a full aperture optical figure that is almost perfect: ~λ/6000 rms, or ~1Å, hence the need for extreme wavefront control and Angstrom accuracy deformable mirrors.

In our nulling coronagraph architecture, we plan to have a fiber array of approximately 1,000 fibers (arranged in an hexagonal array with a diameter of 39 fibers). For TPF-c, light from an 8m/39~ 20cm part of the primary falls on a lenslet which focuses the light into a single-mode fiber. At the output, this light is recollimated. Optically coupled to each fiber is a segmented deformable mirror in one arm of each nulling interferometer. This DM is used to control the amplitude and phase of the light. At the fiber input, if the starlight is suppressed by 10^{-7}, then at the output a total of 10^{-7} of the starlight will appear as scattered light. Because in general the nulling process will produce residual leaked light with random phase, this 10^{-7} starlight will be scattered uniformly over the airy spot output field of view, with an average scattered light level of 10^{-10}/airy spot.

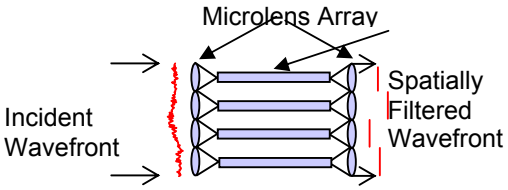

Figure 3 A single mode spatial filter array consists of an input lens array that divides incident wavefront into multiple segments and couple light in each segment into a single mode fiber, which removes higher-order spatial modes from each light segment; a second lens array recollimates the light from each fiber.

2.3. Calibration system-- Impact of the post-SSS (calibration) wavefront sensor

Although starlight is suppressed to 10^{-10}, the resulting speckle pattern needs to be subtracted to a much lower level, 2 x 10^{-11} for a 5 sigma detection of a planet. The post-starlight suppression system (SSS) sensor has two functions. One is to provide real-time feedback to the adaptive optics (AO) system; to correct the state of scattered light, and to make the wavefront more perfect. The second function is to provide post-detection information on the amplitude and phase of this post-SSS wavefront in order to generate an estimate of the post-coronagraph point spread function (PSF) for subsequent correction by software subtraction.

The default TPF procedure for subtracting residual starlight is to roll the telescope around the line of sight after about 2~4 hours of integration. For this method to work, the null has to be stable to 2×10^{-11} for hours, which means that the wavefront must be stable to single digit picometers. With a calibration interferometer, we measure the residual wavefront concurrent during science

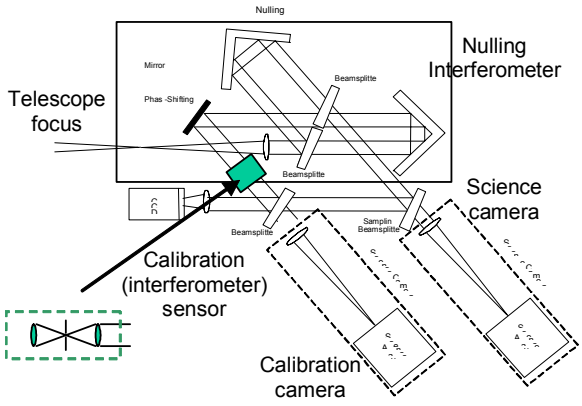

Figure 4. Concept for a calibration wavefront sensor with a nullling coronagraph.

integration. Having both the image and an estimate of the wavefront error, the wavefront stability requirements can be relaxed by 4 to 6 orders of magnitude (picometer (pm) level stability over hours of integration versus pm stability over a fraction of a second).

Wavefront changes caused by nanometer motions of the telescope secondary with respect to the primary mirror generate errors (focus, astigmatism, coma, etc.) that result in scattered light at 2-3-4 λ/D. Making any coronagraph/nuller work at small λ/D is difficult, but the calibration wavefront sensor makes 2 λ/D coronagraphs feasible.

The basic idea of the post starlight suppression system (SSS) wavefront sensor is to use the light blocked by the SSS as a "reference" beam in an interferometer to measure the post SSS electric field, both amplitude and phase. (Variations of this approach have been described by Guyon, 2004.) A Mach-Zehnder Interferometer forms the heart of this concept (Figure 4). It comprises two beams: a reference beam and an unknown. The reference beam is created from the light that passes from the bright output of the first nulling interferometer. The light that forms the second (unknown) part is the nulled light picked off after the fiber array and before the science camera. The two beams are combined in the calibration camera, and using modulation with a 4-bin algorithm, the amplitude and phase of the stellar leakage is computed. The leakage point spread function is estimated by propagating this field into the far-field.

2.4. Performance studies-- Sensitivities and Signal to Noise

We have also developed an extensive suite of IDL-based routines that allow us to generate simulated images under a variety of conditions (Figure 5). It is an image of an earth-like planet with $1.2x10^{-10}$ contrast and at 0.1 arcsec from a G2V star at 10 pc. A 3600 sec integration time per each of the 3 rotations, is assumed, as well as a 600nm to 700nm bandpass. The simulated errors include 0.1 nm phase error, and -photon noise effects on science and wavefront sensor cameras. This image is assumed to be corrected by subtracting an estimated psf as computed from the calibration wavefront sensor camera. It is important to notice that the nulling interferometer provides a relatively high aperture efficiency: 80-90%. In addition, further improvements can be had by adjusting the shear for each star observed to optimize the tradeoff between stellar leakage and effective area.

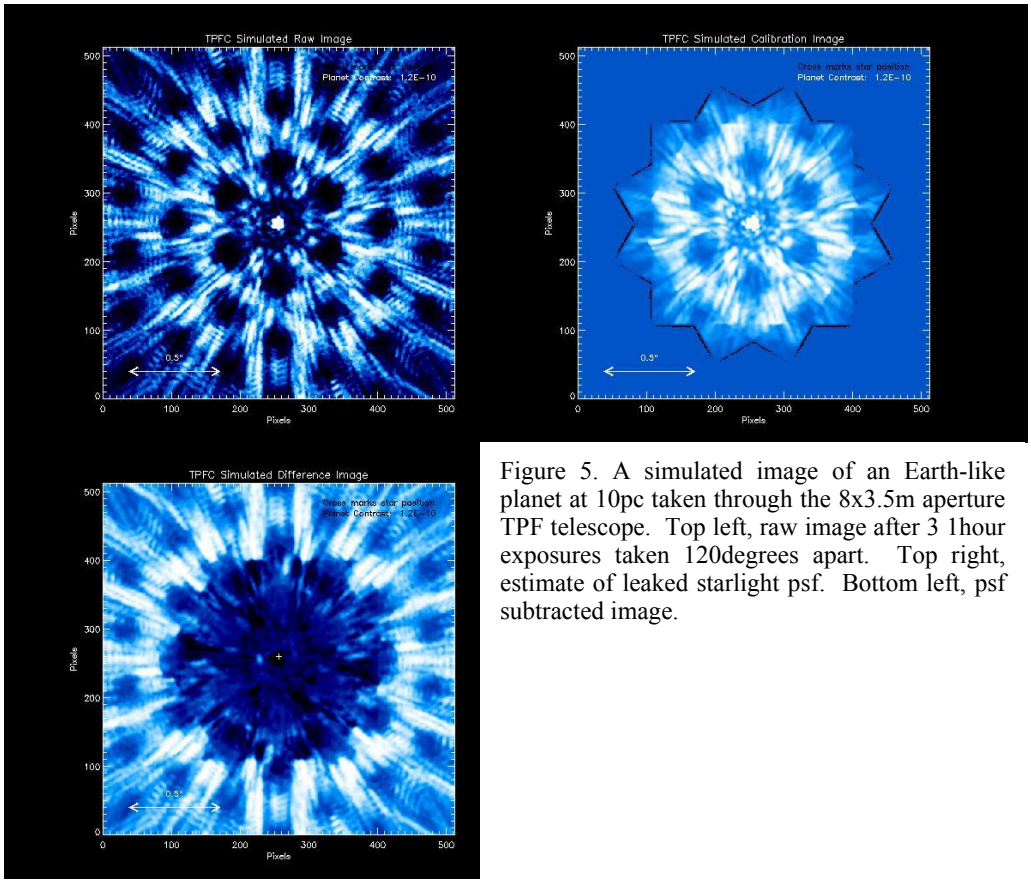

Figure 5. A simulated image of an Earth-like planet at 10pc taken through the 8x3.5m aperture TPF telescope. Top left, raw image after 3 1hour exposures taken 120degrees apart. Top right, estimate of leaked starlight psf. Bottom left, psf subtracted image.

To illustrate the calculations we explored a number of cases, including a canonical Earth-Sun system viewed from a distance of 10pc, a Sun-Jupiter system at the same distance, and finally an Earth-like planet in the habitable zone of an

M star at a distance of 5 pc. We calculated the SNR as a function of wavelength, from 0.5μm to 1.5 μm. These are all given in Table 1 below.

There are three important figures-of-merit to consider; the first and most obvious is the SNR. However, the resolution parameter (in units of Lambda/Diameter of the telescope) is also important, with small values of this parameter being increasingly hard to observe (the limit depends somewhat on the level of low-order optical aberrations in the system, but 2 λ/D is a reasonable limit to consider.) Finally there is the "Q" parameter - the ratio of background flux to planet flux, at the location of the planet. Although this ratio may be less than unity, small values for Q place increasingly stringent limitations on the stability requirements of the system (e.g. wavefront stability). Note however that with the addition of the post-SSS calibration system we can tolerate Q values that are well below unity. In such cases it is no longer the stability of the background flux that sets the detection limit, but rather the photon noise fluctuations in that background that set the detection limits.

Wavelength (μm)		**0.55**	**1.00**	**1.50**
Object	**Quantity**			
Earth, G2V@10pc	**SNR**	**9.76**	**9.81**	**5.34**
	λ/D	**5.06**	**2.45**	**1.42**
	Q	**0.68**	**0.52**	**0.19**
Jupiter, G2V@10 pc	**SNR**	**25.51**	**28.79**	**20.81**
	λ/D	**26.39**	**12.65**	**7.05**
	Q	**2.90**	**3.70**	**1.95**
Earth@0.15 AU	**SNR**	**6.79**	**3.17**	**1.16**
M2V@5pc	**λ/D**	**1.22**	**0.54**	**0.26**
	Q	**0.41**	**0.03**	**0.01**

Table 1: Sensitivity summary for selected star-planet systems. All cases assume a 1 hour integration time and 20% bandpass.

In all our test cases we find that the planets could be seen with high Signal-to-Noise ratios in at least one band. Two noteworthy cases are the 1.5-micron detection of a Sun-Earth configuration (assuming operation at 1.4 λ/D is possible), and the 0.5 μm detection of a habitable-zone planet around an M star.

3. Technology Assessment

3.1. Status of Deep nulling

We used both laser and filtered white light (broadband) sources. For laser sources we used a laser diode module from Melles Griot emitting at 638nm with a pigtailed power capable of 11mW but tuned to 4mW (3.75V, 80mA) for better stability. Broadband nulling was always carried out after laser alignments, and tests. The white light source used was of incandescent (filament) type and installed on a mini bench, equipped with a filter wheel with choice of filters with central wavelength 650nm, then a lens focused the beam on the core of the single mode fiber leading to the nuller. We used the bandpass of 5% and 12%. For bandpass verification we injected the light into a small pigtailed USB2000 spectrometer module from Ocean Optics.

In order to reach very deep nulls, sub-nanometer optical path difference and stability, mechanical stability and vibration isolation, optical alignment and intensity symmetry in the two arms are all needed. The most important factors were OPD noise and power imbalance. OPD noise was easily deduced from measureing the intensity power spectrum ath midfringe using a fast rate (KHz) photodetector. The rule of thumb is that 0.1nm RMS OPD limits the null to 2.5×10^{-7} solely from this contribution. For the power imbalance (mismatch) the intensity in each arm of the interferometer was recorded while the shutters are clicked alternatively, and at a relatively fast rate (every few seconds) compared to laser source (or other) fluctuations. This effect is also quadratic. The required mismatch is ~0.1% for 1M null. Here the rule of thumb is that 0.15% intensity mismatch limits null to 2.8×10^{-7} solely from this contribution. Initial power mismatch could not exceed a few % with good nuller construction and reasonably matched coatings. To fine tune intensities to the 0.1% or better level we used a fine tip tilt control (picomotor) within and outside the nuller. We have

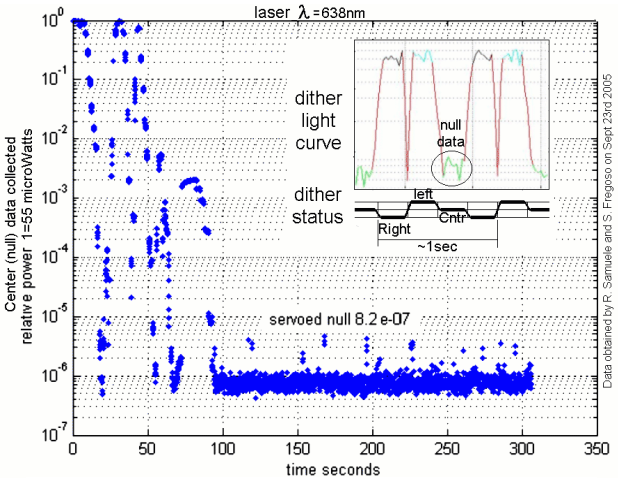

Figure 6: A 1.2million to one servo null..

analyzed our 1M null in terms of OPD noise and intensity mismatch. We found 0.1nm RMS for the OPD noise and 0.15% for the power mismatch. Therefore the sum amplitude and phase errors would be ~$5x10^{-7}$ versus $7X10^{-7}$ measured, so there was one (or more) small error factors in the null depth. Possibly both amplitude and OPD stability could improve by 3~5x if the chamber was pumped, therefore the current experiment could get us to a limit of ~1-$2X10^{-7}$ nulls (~1-$2X10^{-10}$/airy spot). But vacuum operation has not yet been done.

A third factor under recent investigation is angular/polarization mismatch. This parameter is sensed by looking for intensity variations in each arm of the interferometer separately using crossed polarizers. From a geometric point of view we need to align the angle of incidence of optics (about 15deg) to the arcminute level, as well as wedge orientations, and also to pay attention to mirror coatings and pairwise matching of coatings for the beam splitters. We are currently rebuilding the nuller under an autocollimator to the subarcminute level.

3.1.1. SERVOED NULL

A a 1 Million level type laser null is shown in Figure 6. We implemented a servo technique based simply on the signal itself, using the weak flux around null, as opposed to other schemes typically using heterodyne laser metrology to monitor paths (in fact we implemented this a few years ago), or a quadrature output (Serabyn, 1999c). We applied a small OPD dither cycle around the null with 3 plateau positions called left, center (null) and right and monitored the light level at these 3 points. From any difference between the right and left levels we could easily tell any drift away from the null. Under LabView, with the proper conversion factor, we fed back the positive or negative error signal into the piston actuator to bring the null back. In terms of servo parameters we used a relatively slow cycle rate of 1Hz given the low flux (55 µW on top of the fringe, 55pW at null), we had a duty cycle of ~25% (8 null points out of 33), and a dither excursion of ~10nm. The closed loop operation added a minimal amount of noise and did not degrade the original 1Million null. We finally tested correct function of the closed loop by applying small OPD disturbances and verifying that the null would (slowly) come back despite of the very low flux captured at the left and right points.

3.1.2. BROADBAND NULLING

Whereas nulling interferometry is easiest for monochromatic light (laser), scientific and astronomical interest lies only in broadband (star light) capability. The nuller was equipped with tilted glass plates (dispersion plates) as described in the past (Serabyn et. al, 1999a, 1999b, Wallace et. al, 2000) to create varying glass effective thickness between the right and the left arm. To date, we have experimented only one glass type per arm, but have plans to install two glasses (two plates) per arm to augment bandwidth. For broadband visible performance the glass effective thickness (ie the plate angle, given a certain physical thickness and refraction index) difference between left and right arms was calculated to be 20micron in theory, with about 29micron of extra air in the other arm to compensate. Empirically we adjusted the angles of the right versus the left plate, using rotary picomotors, to symmetrize the +1 and -1 fringe on each side of the white-light null (symmetry of the fringe packet). When exploring the 'rotation fringe' space, we found nulls regularly spaced, deeper nulls surrounded by higher order nulls. With two glasses the procedure will be much more complex and the difference of effective thickness would theoretically be ~400µm.

Using this method of tuned plates in interferometer, in air, without polarizers, with filtered red light at center wavelength of 650nm, we found the following results: the nulls were found to be 120000 for 5% bandpass, and 32000 for 12% bandpass (Figure 7)

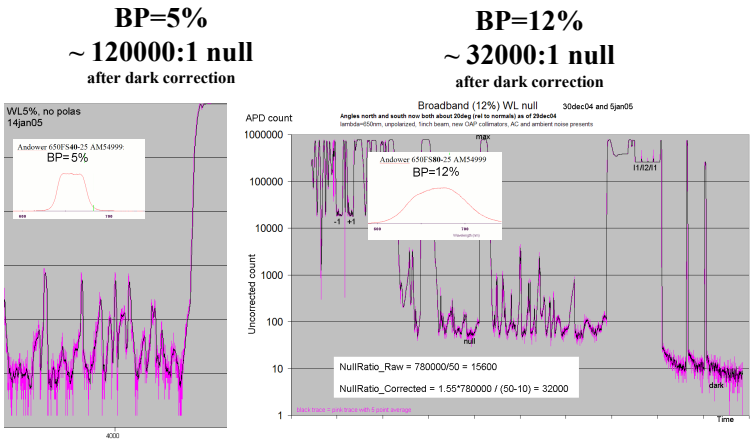

Figure 7: Experimental White Light Nulling Results

3.2.

Spatial filter technology (fiber arrays, pinhole arrays)

A single mode spatial filter array consists of a coherent fixed-length fiber array sandwiched by two lenslet arrays as shown in Figure 3. Approximately 1000 fibers are needed in the array for implementing nulling imaging of planets. We have developed a visible wavelength single mode fiber array using precision prisms to confine the fibers in a hexagonal pattern and a method to align the fiber array to a custom lenslet array using a Zygo interferometer and a 6-axis stage. To reduce the alignment sensitivity we used a custom large mode field diameter (~9μm) single mode fiber. The off-the-shelf visible wavelength single mode fiber has a core diameter of 3.5μm and has a very tight alignment tolerance. A fiber position mapping method is also developed for the lens array design.

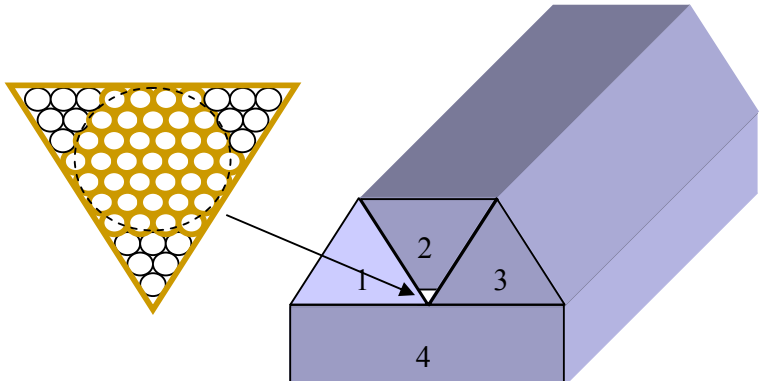

Figure 8 Fiber array is made by confining fibers by equilateral prisms 1 and 3 and equilateral prism 2 with one vertex beveled (polished off) to have a width given by that of the fiber array plus the diameter of one fiber.

3.2.1. Fiber Array

The design of the fiber array is based on the use of 3 precision equilateral prisms placed on a flat base plate as shown in Figure 8. The middle prism has one of its vertices polished flat to a width approximately equal to the side length of the fiber array to be built. The fiber array is confined by two facing sides of the upright prisms and the flat top of the middle prism. The width in the bevel of the middle prism is polished to be approximately one fiber diameter greater than the side length of the fiber array. This ensures that the middle prism touches and confines the fiber array from the top. To limit the coupling loss caused by misalignment to a maximum 10% efficiency drop or a 2 μm offset, the maximum angular offset of a 1027 effective hexagon in a 1540 triangular array using 300 μm cladding diameter fiber, is ~ 20 arc seconds. This is the tolerance specification for the vertex angle of the equilateral prisms. The bottom of the prisms when placed on the base flat also need to be parallel with each other by 20 arc seconds. This can be controlled by observing the interference fringes generated between the prism base and the base flat. We used a prism with a height of 15 mm. The maximum number of fringes in visible wavelength is approximately 3.

When the longer sides of the prisms are not parallel with each other, the fiber array will see a triangle formed by the 3 prisms deviated from being equilateral. If we impose the same 20 arc second tolerance requirement on this triangle, it can be calculated that the longer sides of the prisms need to be parallel with each other within 2.42 degrees. However, another restriction is that the gap created by this needs to be less than the diameter of the fiber, otherwise the bottom fiber will slip through the gap. For example, for a fiber with a cladding diameter of 300 μm and a prism length of 72cm, the maximum angle between the two long sides of the prisms is 1.43 arc minutes, which is much smaller than the 2.42 degree tolerance mentioned above. However, in order to use the prism for measuring the perpendicularity between the fiber and its end faces the fiber needs to be perpendicular to the end face of the prism within 20 arc seconds. This requires the two long sides of the prism to be parallel within 22 arc seconds. For a 72cm long prism, this means the gap between the two prisms at the base needs to be < 80 μm. As a result, the criteria for determining if the two prisms are placed parallel enough visually to make sure the gap between the bases of the two prisms be smaller than ¼ of the fiber diameter on two ends of the prism assembly. In order to use the prism as the reference for controlling the perpendicularity of the fiber end face the prism also needs to be the reference when the two ends of the fiber array are polished. The outer geometry tolerance discussed above controls the systematic error. However, it does

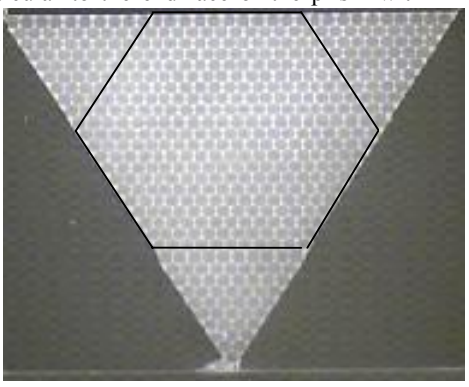

Figure 9 Polished end of the 125μm diameter, large core 496/331 (triangle/hexagon) fiber array.

not control the random error caused by the concentricity of fiber core and cladding and the fiber cladding diameter. For the standard 125 μm and custom 300 μm cladding fibers, the concentricity tolerances are 0.5 and 1.5 μm, respectively. The cladding diameter can be very uniform if the fiber segments are cut from the same section of a fiber lot. Thus the larger the cladding diameter the larger the random error will be in the fiber spacing. In general, the spacing variation can be on the order of 3 μm for the 300 μm cladding fiber. This will cause the coupling efficiency to drop 30% from the peak value.

3.2.2. Microlens Array

Commercial micro-lens array such as epoxy molded and gray-scale photolithography etched fused silica lens arrays are being used in this work. In general, the former has a center to center spacing tolerance of 1 to 2 μm, while the latter of 0.5 μm. If the lens is designed on the side facing fiber array, the distance between the lens array and the fiber array can be controlled by a precision spacer. If the lens is designed on the side of the substrate opposite to the side facing the fiber array, the distance between the lens array and fiber array is controlled by the thickness of the substrate or a substrate plus a precision spacer. The former is used in with the epoxy molded lens array and the latter is used in with the gray-scale photolithography etched lens array. The advantage of the latter is index matching epoxy can be used to bond the lens array and fiber array and this in turn reduces the wavefront distortion that can be caused by the irregular surface on the fiber array.

A U Florida group (McDavitt et. al., 2004) uses precision V-grooves etched in silicon to hold fibers with large mode field diameters (MFD) in precise alignment to one another and they stack layers of these V-grooves with fibers to form a 2-D fiber array. The silicon serves as a support to the fibers, not pressing down on them but merely holding them into position.

3.2.3. Fiber position mapping

A lens array on the alignment fixture is positioned to couple its focused light (and not necessarily be optimal alignment) into each of the fibers. A CCD camera with an image relay system records the spot pattern. An aperture stop is placed at the pupil plane to control the f/number of the optical system. Changing the f/number controls the diffraction spot size and the number of pixels per diffraction spot on the CCD camera. For our 19 mm diameter stop, the FWHM width of the spot is about 3 to 4 pixels.

A measure of array regularity is calculated by the rms difference between these measured centroid positions and the theoretical positions of a regular array with constant spacing (see Figure 10). The imaging system is calibrated with a reference transmission array made using an e-beam photolithography machine. The placement accuracy is much less than 0.1 μm or two orders of magnitude better than the placement accuracy of the fiber array.

The largest array built is a 496/331 (triangle/hexagon) fiber array (Figure 5.14) using a custom ~9 μm mode field diameter (MFD) single mode fiber at 500 nm wavelength. The cladding of the fiber is 126 μm nominally. The spacing uniformity of these fiber arrays is much better than that of the fiber arrays reported in Liu et. al., (2003, 2005) due to an improvement in the fiber laying process.

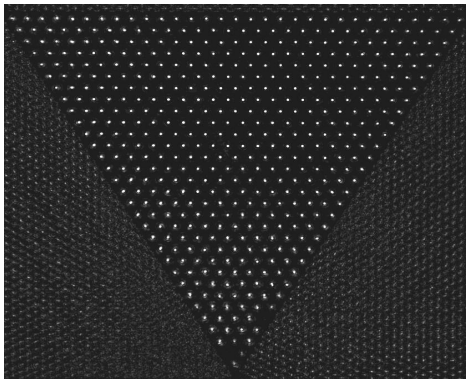

Figure 10 Light output of the large core 496/331 fiber array when a collimated HeNe laser beam is coupled into the array via a lens array. The output end does not have a lens array.

3.2.4. Future Work

We plan to align and bond the lens array to the large core fiber array reported in this work and characterize the wavefront distortion caused by this array. In addition, we plan to build another 496/331 (triangle/hexagon) fiber array using a 300 μm cladding diameter and 12 μm mode field diameter single mode fiber with a cutoff wavelength of 500 nm. The 300 μm cladding diameter is chosen to match half of the spacing of the deformable mirror to be used in a future system demonstration. Due to limitations in the fabrication capability as the cladding diameter increases the concentricity of the fiber core can decrease. For the 125 μm cladding fiber used in this work, the core-cladding offset of the fiber is 0.5 μm, while for the 300 μm one, it is 1.5 μm according to the manufacturer's specification. To reduce the impact of this increase in core-cladding offset, we will also explore the possibility of mapping the individual fiber

position and then use it to fabricate a custom lens array with matched positions, and to improve the uniformity of coupling efficiency.

3.3. Segmented Deformable Mirror (Stewart, et. al. 2006)

A schematic and summary for the new DM design can be seen in Figure 11, consisting of 329 discrete hexagonal mirror segments, each supported by three independent electrostatic actuators from two different actuator rows. The three actuators are connected to the hexagonal mirror segment via posts that resemble vertices of an equilateral triangle. These actuators are identical to those exhibited in a 'conventional' MEMS deformable mirror, but every other row is now offset by a length equal to half the actuator span. This actuator geometry provides the mirror with tip, tilt, and piston motion. The microfabrication process for the TPF DM begins with a three-layer polysilicon surface micromachining process (similar to the inherited process) involves the deposition and patterning of alternating layers of sacrificial and structural thin films). The 1st and 2nd polysilicon layers in the process developed are 500nm and 2μm thick, respectively, and the two sacrificial oxide layers are 5μm thick. The 3rd polycrystalline silicon layer, which used to be the final mirror surface, is 3μm thick and it is used as a seed layer for a thicker epitaxial grown polysilicon layer. The purpose for this epi-polysilicon layer is to add rigidity to the mirror segment and aid in the chemo-mechanical polishing of the mirror surface to achieve the surface roughness needed for the nulling coronagraph. Other process modifications used to improve mirror optical quality include the removal of oxide etch-access holes on the mirror surface to reduce diffraction effects, and the addition of a polishing step after the 2nd oxide deposition to reduce print-through from the patterned layers below.

A significant challenge in the design of the TPF DM was the development of a mirror segment that remains rigid during actuation. A thin mirror layer, such as the 3μm thick polysilicon mirror layer of the inherited DM technology, will bend during actuation due to moments applied through the actuator post attachments to the mirror segment. If the thickness of the mirror segment is increased, or if the electrostatic actuators for the segment are decoupled from the mirror surface, bending can be reduced to a level acceptable to the nulling coronagraph. Finite element modeling of the TPF DM design led to two acceptable architectures that are based on these principles. The first architecture uses conventional actuator designs and a mirror segment layer thick enough to resist bending moments introduced by the rigidly attached electrostatic actuators during tip/tilt motion. The epitaxial growth of polysilicon on the mirror surface (as described above) is capable of achieving a range of thicknesses. According to the finite element modeling results, the thickness critical to reduce mirror bending to an acceptable level was found to be 15μm.

The second architecture developed decouples mirror segment tip/tilt motion from the deflection of its electrostatic actuators. This is performed by etching flexure cuts in the compliant actuator diaphragm, encircling the post connection to the mirror segment, giving the mirror post freedom to move with the mirror segment as it tips and tilts. This reduces the bending moment imparted to the mirror segment by the mirror post. The flexure design is also known as the gimbal actuator design because it resembles a two-axis gimbal, as can be seen in Figure 12. Using a flexure actuator with low torsion resistance, a mirror segment thickness of approximately 4μm would be sufficient to satisfy coronagraph figure requirements, compared to the 15μm without flexure actuators. As will be discussed, by reducing the mirror segment thickness, mirror curvature due to residual stresses becomes more manageable. A thick mirror segment that is curved due to residual stresses is more difficult to flatten via post-processing than a thinner mirror.

The nulling coronagraph requires that the DM segments have a radius of curvature greater than ~5m, and that mirror

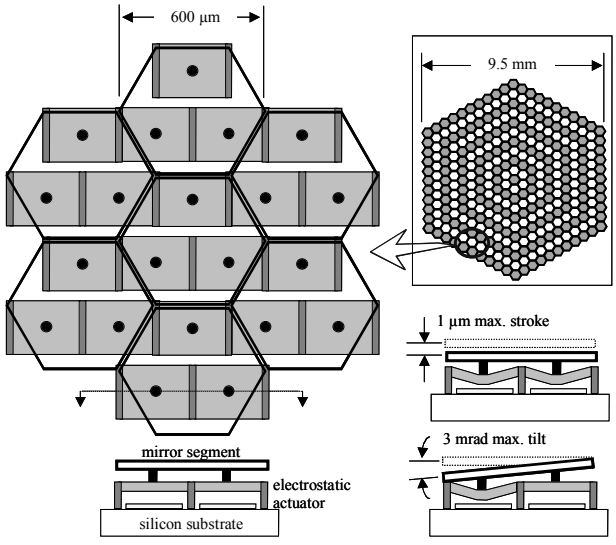

Predicted DM Performance	
Mirror architecture	329 close-packed hexagonal segments
Actuation architecture	Electrostatic tip/tilt/piston control for each segment
Mirror segment geometry	600μm hexagon, with epitaxial polysilicon layer for mirror rigidity
Mirror segment material	Silicon, 1000 Å gold coating, near-IR and visible
Segment motion (piston)	1 μm range, 0.1nm resolution
Segment motion (tip/tilt)	600 arc-second range, 0.06 arc-second resolution
Segment flatness	Surface roughness < 1 nm RMS Figure < 1 nm RMS Radius of curvature > 5 m

Figure 11: Top and side view of the new MEMS TPF DM architecture for tip/tilt and piston motion (left). Table summarizing predicted DM performance (right).

segment surface roughness be less than 10nm rms. As one can see in Figure 13, the optical quality of the polished, epitaxial grown, polysilicon DM segment is somewhere between these specifications. Due to significant tensile stress gradients in the 15µm thick polysilicon mirror layer, the DM segments are cup shaped and have an average radius of curvature of 270mm. However, if the curvature of the mirror is neglected, the mirror segment has a 5nm rms surface roughness (near the noise threshold of the measuring interference microscope), which satisfies the requirement.

The most significant task remaining for the successful fabrication of a segmented DM is the development of a method to produce flat mirror segments. A method to fine tune mirror curvature after the DM is released has been demonstrated by BU, but it requires a thinner DM segment with tensile stress gradients. The process uses the implantation of inert gases in the mirror surface to create a thin film of compressively stressed material that acts to flatten the mirror segment. If the flexure actuator design is used, the final mirror segment thickness will be on the order of 4µm, which is within range of this technique. Furthermore, if the flexure actuator design succeeds, it may also be possible to fine tune tensile stress gradients through the deposition of compressively stressed thin films, such as the final reflective metal coating. Lastly, process development to reduce stress gradients in epi-polysilicon layers of various thicknesses using high temperature furnace annealing is underway. High temperature annealing of thin polysilicon films to reduce stress gradients has been successful in other MEMS applications (Zhang, 1998) and has been used for the production of flat DMs in the inherited BU fabrication process. (In addition stability of this actuator has been measured to be within a standard deviation of 38pm (Gavel, et. al, 2005)

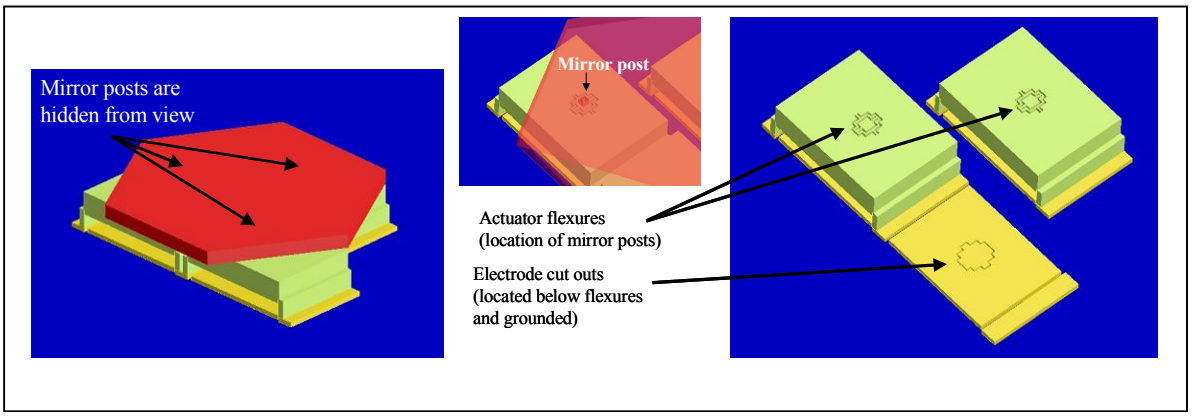

Figure 12: 3D model of the flexure (gimbal) actuator design. Full model (left), location of mirror post (center), and view of flexure cuts in actuator diaphragm with mirror segment removed (right). Designs with and without electrode alterations are currently being explored.

3.4. Deformable Mirror electronics (Figure 14)

No affordable, commercially available electronics were available capable of producing 1024 analog voltages. Working with Analog Devices Inc., we developed a set of electronics for driving deformable mirrors that will be suitable to many applications. Based on the new AD5535 chip, a modular deformable mirror controller board has 128 independent high voltage, 14 bit digital-to-analog converters, each driving a single deformable mirror pixel.

These electronics have been demonstrated with a MEMS deformable mirror from Boston Micromachines, using

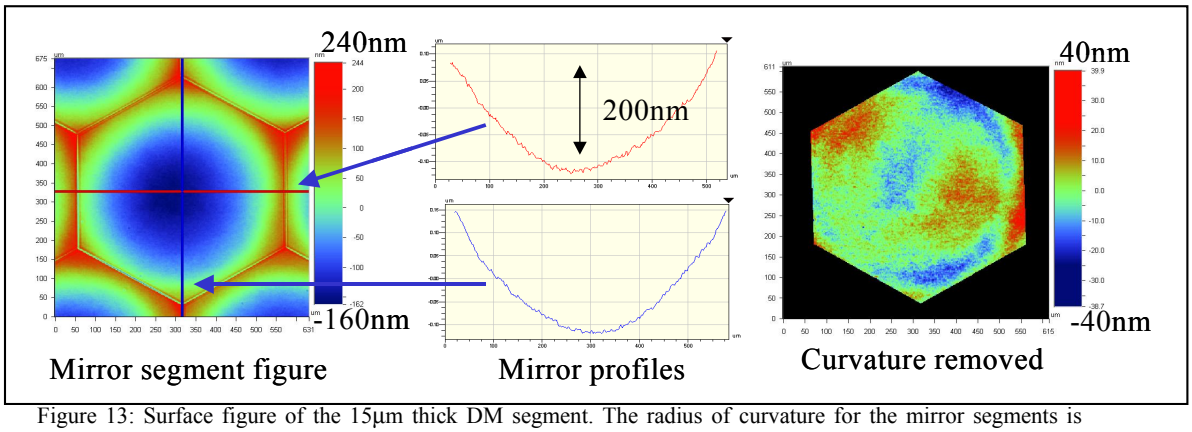

Figure 13: Surface figure of the 15µm thick DM segment. The radius of curvature for the mirror segments is 270mm (left). Neglecting mirror curvature, the mirror segment roughness is 5 nm RMS (right).

automated procedures for characterizing and calibrating each individual mirror actuator. For a square-law DM with a range of 2 microns, the high resolution of the AD5535 chip gives a displacement resolution better than 3A.

This system is currently configured for use in the laboratory, with inexpensive USB or parallel-port interfaces. The time to update all 128 channels is approximately 240usec from a standard PC.

4. Summary

We have described a starlight suppression architecture capable of detecting earth-like planets at 2λ/D angular resolution, and have presented its signal to noise ratios for various objects. The overall suppression depends on interferometric starling cancellation, spatial filtering with a coherent single mode fiber array, amnd by causing calibration wavefront sensing. Using a modified Mach Zender interferometer as our nuller testbed we have developed technologies and experimental progress to reach very deep nulls needed for future planet detecting missions. Using visible laser light (638nm) we have achieved a 1.2 Million (average raw null over many seconds), and under unpolarized filtered white light at 650nm, and using one glass plate in each arm, we obtained a null of 120000 with a bandpass of 5%, and 32000 with a larger bandpass of 12%. Moreover we report a latest result of closed loop nulling: we have been able to track the laser null ,with a slow bandwith and with little noise degradation.

We have demonstrated the feasibility of fabricating a single mode fiber array with 496 fibers in a triangle or 331 fibers in a hexagon confined by 3 precision prisms with light coupled across the entire fiber array. This is feasible with the use of a custom large mode field diameter fiber, which greatly relaxes the lens array to fiber array alignment sensitivity. The tolerance analysis shows it is possible to build a 1540/1027 (triangle/hexagon) lens-fiber array with 15% fiber coupling efficiency variation. This will make it possible to detect extrasolar earth-like planets in nearby stars using a nulling interferometer with a 10 million to 1 contrast ratio.

Significant progress has been has been made in the fabrication of segmented deformable mirror and their associated driving electronics. A process for builing the segmented DM has been derived from previous commercial designs. The concept of using flexured actuators beneath each segment has been demonstrated. Current experiments are now underway to determine an acceptable thickness for the top epi-poly silicon layer that allows for minimal segment roughness, and also for the required flatness. A set of electronics, using commercial parts, have been fabricated that will drive this mirror.

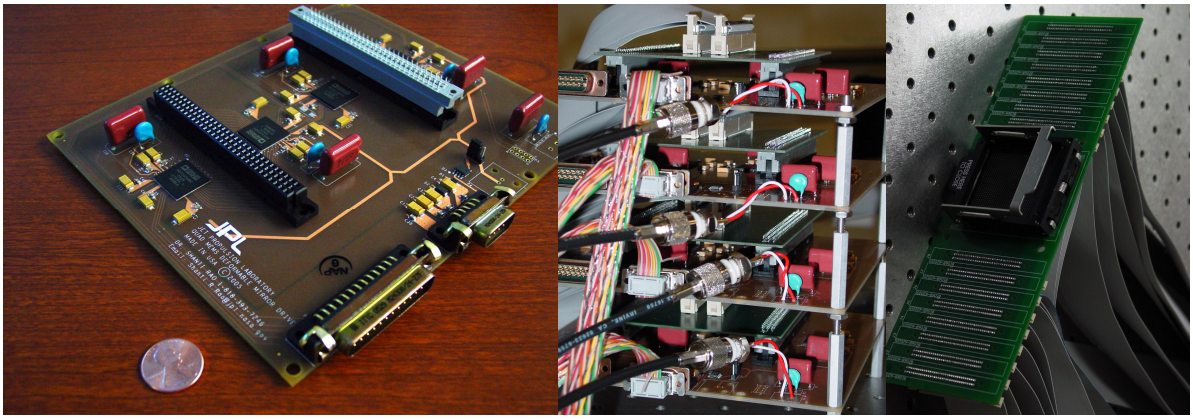

Figure 14: Left, A circuit board with 128 channels of voltage output. Center, An assembly of 4 of 8 boards set up for a laboratory demonstration. Right, ZIF socket for 1000 actuator deformable mirror

Acknowledgements

This work was performed at the Jet Propulsion Laboratory, California Institute of Technology, under contract to the National Aeronautics and Space Administration.

5. References and Bibligoraphy

1. Angel, R., (1990), "Use of a 16-m Telescope to Detect Earthlike Planets," Proceedings of the Workshop on The Next Generation Space Telescope, P. Bely and C. Burrows, eds., Space Telescope Science Institute, pp. 81–94.

2. Angel, J.R.P, and Woolf, N.J., (1997),"An Imaging Nulling Interferometer To Study Extrasolar Planets,"Astrophysical Journal, v475, pp. 373-379.

3. Shao, M.,(1991), "Hubble Extra Solar Planet Interferometer", SPIE v1494.

4. Morgan, R., Burge, J., and Woolf, N., (2000), "Nulling Interferometric Beam Combiner Utilizing Dielectric Plates" Experimental Results in the Visible Broadband SPIE v4006.

5. Serabyn, E. and Colavita, M.M., (2001), "Fully Symmetric Nulling Beam Combiners", Applied Optics, v40, pp. 1668–1671.

6. Mennesson, B.P., Shao, M., Levine, B.M., Wallace, J.K., Liu, D.T., Serabyn, E., Unwin, S.C., Beichman, C.A., (2002), 'Optical Planet Discoverer: how to turn a 1.5m class space telescope into a powerful exo-planetary systems imager', SPIE, v4860.

7. Shao, M., Serabyn, E., Levine, B.M., Mennesson, B.P., and Velusamy, T, (2002), 'Visible nulling coronagraph for detecting planets around nearby stars', SPIE v4860.

8. Levine, B.M., Shao, M., Liu, D.T., Wallace, J.K., and Lane, B.F., (2003), "Planet Detection in Visible Light with a Single Aperture Telescope and Nulling Coronagraph", SPIE v5170.

9. Liu, D.T., Levine, B.M., and Shao, M, (2003), "Design and fabrication of a coherent array of single-mode optical fibers for the nulling coronagraph", Proc. SPIE Vol 5170.

10. Wallace, .K., (2004), "Experimental Results from a Visible Nulling Interferometer", Proc IEEE Big Sky Conference.

11. Liu, D.T., Levine, B.M., Shao, M., Aguyao, F., (2005), "Single Mode Fiber Array for Planet Detection using a Visible Nulling Interferometer", Proc. IEEE Big Sky Conference.

12. Ge, J., McDavitt, D., & Miller, S., 2004, "Development of an extremely coherent single mode fiber bundle array for high contrast imaging of extrasolar planets with visible Terrestrial Planet Finder", Proc. SPIE, 5491.

13. Schmidtlin, E. S. , Wallace, J.K., , Samuele, R, Levine, B.M., and Shao, M., (2005), "Recent progress of visible light nulling interferometry and first 1 million null result", Direct Imaging of Exo Planets, Proceedings IAUC200, Nice, October 3-7th, 2005.

14. Stewart, J.A., Bifano, T.G., Bierden, P., Cornelissen, S., Cook, T., Levine, B.M.,(2006), "Design and development of a 329-segment tip-tilt piston mirror array for space-based adaptive optics", SPIE 6113-24.

15. Zhang, X., Zhang, T., Wong, M., and Zohar, Y. (1998) , "Rapid thermal annealing of polysilicon thin films" J. Microelectromechanical Systems 7, 356.

16. Mennesson, B., Ollivier, M., Ruilier, C., Use of Single-Mode Waveguides to Correct the Optical Defects of a Nulling Interferometer, (2005), JOSA, Vol 19, No. 3, March 2002.

17. Schmidtlin, E., Wallace, J.K., Samuele, R., Levine, B.M., and Shao, M., (2006), "Recent progress of visible light nulling interferometry", Proceedings of IAU, Conf 200, C. Aime, Editor.

18. Serabyn, E., Wallace, J. K., Nguyen, H. T., Schmiditlin, E. G. H., Hardy, G. J., (1999), in Working on the Fringe: Optical and IR Interferometry from Ground and Space (eds Unwin, S. & Stachnik, R.) 437-442.

19. Serabyn, E., Wallace, J. K., Hardy, G. J., Schmidtlin, E. G. H., Nguyen, H, (1999), Deep nulling of visible laser light, Appl. Opt. 38, 7128-7132.

20. Wallace, K. , Hardy, G., Serabyn, E., 'Deep and stable interferometric nulling of broadband light with implications for observing planets around nearby stars', (2000), Nature, August 2000, 406, 700 - 702.

21. Serabyn, E., (1999), 'Nanometer-level path-length control scheme for nulling interferometry', Appl. Opt. 38, 4213-4216.

22. Guyon, O., (2004), 'Imaging Faint Sources Within A Speckle Halo With Synchronous Interferometric Speckle Subtraction', ApJ, v 615, p562.

23. D. Coulter, (2004), “NASA’s Terrestrial Planet Finder Missions”, Proc. SPIE, v5487.
24. M. Shao, (2006), “A nulling coronagraph for TPF-C”, Proc. SPIE, 6265-4.